Simulation of inviscid compressible multi–phase flow with condensation

Philip Kelleners †

Condensation of vapours in rapid expansions of compressible gases is investigated. In the case of high temperature gradients the condensation will start at conditions well away from thermodynamic equilibrium of the fluid. In those cases homogeneous condensation is dominant over heterogeneous condensation. The present work is concerned with development of a simulation tool for computation of high speed compressible flows with homogeneous condensation. The resulting flow solver should preferably be accurate and robust to be used for simulation of industrial flows in general geometries.

1. Introduction

A substance below its critical temperature can be present in either gaseous or liquid phase, depending on the pressure, and is referred to as a vapour. Vapours present in a mixture of gases and vapours, when subjected to expansion can condensate and form liquid droplets. This phenomenon is observed in e.g. aircraft tip vortices and in industrial flows like steam turbines. Condensation in flows of gas mixtures at high speed has been investigated by, among others; Wegener (1969), Hill (1966), Campbell (1989), Schnerr et al. Schnerr (1996), Dohrmann (1989), Mundinger (1994), Adam (1996) and van Dongen et al. Luijten (1999), Luijten (1998), Prast (1997) and Lamanna (2000). Expansion in nozzles of gases to supersonic speeds has often been used to investigate the physics of condensation. Condensation in the flow around airfoil sections and in steam turbines has been investigated to a large extent. At the University of Twente a numerical tool has been developed to simulate transonic flows with condensation in confined geometries. The solver operates on the basis of a finite volume method using unstructured meshes. It has been observed that results obtained with the solver are very sensitive to accurate shock prediction, and fine shock resolution in the flow field, especially in cases of strong interaction between the gasdynamic shock and the condensation process. The focus of the present work is to improve the accuracy and robustness of the flow solver by improving solid wall boundary treatment and spatial reconstruction for simulations with second order spatial accuracy.

2. Physics of Condensation during Rapid Expansion

Below its critical temperature, a fluid can be in gaseous or liquid phase. The thermodynamical region of coexistence of vapour and liquid in equilibrium in bulk substances is given by the Clausius-Clapeyron relation. For rapid expansions of vapour this coexistence region is passed without the fluid attaining equilibrium. The vapour is saturated expressed by the saturation ratio;

† Address: Engineering Fluid Dynamics, Mechanical Engineering - University of Twente, P. O. Box 217, 7500 AE Enschede, The Netherlands

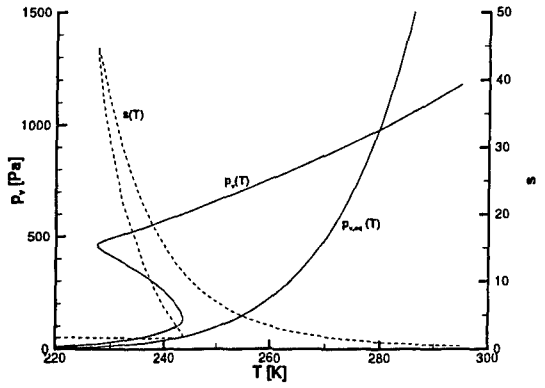

FIGURE 1. Expansion of air–water mixture in nozzle–S2, partial vapour pressures and saturation ratio s (dashed)

$$s = \frac{n_v}{n_{v,eq}} \tag{2.1}$$

where n_v and $n_{v,eq}$ are the number of moles of the vapour in the actual mixture and the mixture in equilibrium, respectively. For pressures as high as atmospheric pressure equation 2.1 can be replaced by the more conventional expression:

$$s = \frac{p_v}{p_{v,eq}} \tag{2.2}$$

where p_v is the actual partial vapour pressure in the mixture and $p_{v,eq}$ is the equilibrium partial vapour pressure at the same thermodynamic conditions. s, p_v and $p_{v,eq}$ are plotted in figure 1 for the expansion of an air–water mixture, as functions of temperature.

The curve for the coexistence of liquid and vapour ($p_{v,eq}$) divides the plane given by pressure and temperature into two regions. For pressures higher than the coexistence pressure the substance under consideration (water) is present in liquid form while in equilibrium state. For lower pressures the substance will be present as water–vapour while in equilibrium. The expansion in the nozzle, as given by the partial vapour pressure p_v, is so quick that the water–vapour will not immediately condense under equilibrium conditions. This is the case as the characteristic time of the gasdynamic flow is much smaller than the time needed to form the first onsets of the new liquid phase. For the nozzle flow at hand this is due to the high–cooling rate in the nozzle. So the water–vapour expands further, driving the air–water–vapour mixture well away from equilibrium, as indicated by the saturation ratio which attains values as high as 40. In case $s > 1$ the fluid is said to be super–saturated. Formation of small liquid clusters, nuclei, at high super–saturation is the first stage of the condensation process that starts in order to reestablish equilibrium. On these newly formed nuclei, the super–saturated vapour condenses as a second step until equilibrium is reached, the process of droplet growth. This can be seen in figure 1 by the decrease in partial vapour pressure and the increase in temperature. With so much liquid already present, the remainder of the condensation process due to droplet growth takes place very close to thermodynamic equilibrium of the water, indicated by the saturation close to one, for the remainder of the expansion.

The process described above is the process of homogeneous condensation. In contrast, the process of heterogeneous condensation is droplet growth on foreign, already present particles. However, for high cooling speeds and consequentially high super–saturation the number of new nuclei formed exceeds any realistic number of foreign particles by several orders of magnitude. For the present applications only homogeneous condensation processes are of importance.

An effect resulting from condensation is the release of latent heat during the condensation process, indicated by the increase in temperature during condensation in the previous example of nozzle flow. The latent heat L is defined as

$$L = h_v - h_l \tag{2.3}$$

with h_v and h_l the enthalpy of the gaseous and liquid phase, respectively. The latent heat is the enthalpy needed to evaporate a unit mass of liquid. It is a material property.

3. Nucleation and Droplet Growth models

From the previous treatment of condensation during rapid expansion, it is observed that the condensation process consists of two consecutive stages. The first one is the formation of liquid nuclei, nucleation, the second one is the condensation of vapour molecules on the already present nuclei, making these grow in the process of droplet growth. In the following, a brief treatment is given of the physical background of both nucleation and droplet growth together with the presentation of the models used to simulate these processes.

3.1. *Nucleation*

Under super–saturation vapour molecules can condense on liquid already present or on foreign objects. In the absence of both, the vapour molecules can form small clusters. As a result of the clustering, an additional phase needs to be formed, the interface between the liquid inside the cluster and the gas outside of the cluster. The interface can be regarded as infinitely thin. At the interface there is surface tension. Thus the creation of an interface requires energy. For very small clusters, the surface effects are dominant over volume related effects. As a result the formation of the interface represents an energy barrier in the formation process of the nucleus. If the energy involved in the clustering of the vapour molecules is less than required in the formation of the interface surface, the cluster will disintegrate immediately following its formation. Therefore at near equilibrium conditions, super–saturations close to one, it is highly unlikely, that a realistic number of stable nuclei in a volume at macro scale will be formed although clusters are constantly formed and falling apart. The previous notion results in formulation of formation enthalpy of critically sized stable nuclei, and the number densities in which these stable nuclei are likely to come into existence. The creation enthalpy of one liquid droplet under equilibrium conditions is given by Dohrmann (1989):

$$\Delta G = 4\pi r^2 \sigma - nkT \ln(s) \tag{3.1}$$

where, ΔG is the change in Gibbs enthalpy, r is the radius of the droplet, σ is the droplet surface tension in a plane with no curvature, n is the number of molecules in the droplet, k is the Boltzmann constant, and T is the temperature. In accordance with classical nucleation theory, we note that a stable nucleus will be created when the function for ΔG attains a local maximum. ΔG at this maximum is:

$$\Delta G = \frac{4}{3}\pi r^{*2}\sigma \tag{3.2}$$

with r^*, the radius of this critical sized droplet being given by:

$$r^* = \frac{2\sigma}{\rho_l R_v T \ln(s)} \tag{3.3}$$

where ρ_l is the density of the liquid in the droplet, and R_v is the gas constant of the vapour. The number of droplets created is given by the nucleation rate. For the nucleation rate several models are available, Classical Nucleation Theory CNT–model (Wegener 1969) and the Internally Consistent Classical Theory, ICCT–model (Luijten 1998). In the present work, the CNT–model is applied:

$$J = \frac{\rho_v^2}{\rho_l}\sqrt{\frac{2\sigma}{\pi m^3}}\exp\left(-\frac{16\pi}{3}\frac{\sigma^3}{m\rho_l^2 R_v^3 T^3 \ln^2(s)}\right) \tag{3.4}$$

where ρ_v is the density of the vapour and m is the mass of one vapour molecule.

3.2. *Droplet Growth*

The droplet growth model to be applied depends on the regime in which droplet growth takes place. For pressures of the order of atmospheric pressure droplet growth is based on a balance between condensation of vapour molecules onto droplets, and evaporation of vapour molecules from the droplet. For pressures 1 to 2 orders of magnitude higher, droplet growth is diffusion–controlled. In the present work, high pressure effects are not taken into account. Therefore the Hertz–Knudsen droplet growth model (Hill 1966) can be applied. The droplet growth rate is:

$$\frac{dr}{dt} = \frac{\alpha}{\rho_l}\left(\frac{p_v}{\sqrt{2\pi R_v T}} - \frac{p_{s,r}}{\sqrt{2\pi R_v T_d}}\right) \tag{3.5}$$

where α is an accommodation coefficient usually taken equal to one, T_d is the droplet temperature in the present work equal to the surrounding gas temperature and $p_{s,r}$ is the partial super–saturated vapour pressure over a curved radius of curvature r given by:

$$p_{s,r} = p_{v,eq}\exp\left(\frac{2\sigma}{\rho_l R_v T r_{hl}}\right) \tag{3.6}$$

where r_{hl} is the Hill droplet radius. This radius is computed as an averaged radius over the complete population of droplets at hand. This radius, of course, depends on the distribution function of the droplets.

4. Description of the Liquid Phase

Until now only, the creation and growth rate of a single droplet, and the creation rate, nucleation rate, of new droplets has been treated. Next to that, the size and form of individual droplets and the size and distribution of the droplet population need to be computed. As the number of droplets in the flow cases at hand typically range between 10^{12} and 10^{22} number of droplets per unit mass, it is impossible to describe individual droplets. One alternative approach is to define classes of droplets of similar radius, the class–model. This approach naturally extends to a description of the distribution of the

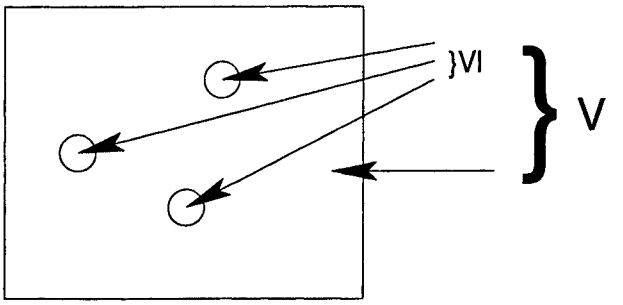

FIGURE 2. Liquid droplets in control volume

droplets. For the nozzle flow problems at hand, the typical range of radii of the droplets will be between 2.10^{-10} and 1.10^{-7}. This would require an impractical high number of droplet–classes, making the class–model computationally very expensive. Hill's method of moments is computationally less intensive at the cost of some of the resolution of the droplet distribution. As for the problems at hand, the total amount of liquid generated and the strong interaction between the gasdynamic flow and the condensation process is of primary interest, the loss of resolution of the droplet distribution is no severe penalty.

4.1. *Hill's Method of Moments*

Consider a control volume as depicted in figure 2. In the control volume a mixture of an ambient gas, and a vapour in its gaseous and its liquid state is present. A first assumption is that all liquid is present in the form of spherical droplets. Conservation of the mass in the control volume gives:

$$M = M_a + M_v + M_l \tag{4.1}$$

where M is the total mass in the control volume, M_a is the mass of the ambient gas, M_v is the mass of the condensible substance in gaseous form and M_l is the mass of the same substance in liquid form. The ambient air is assumed to be permanently above its critical temperature. The dimensionless liquid mass fraction g is defined as:

$$g = \frac{M_l}{M} = \frac{\rho_l V_l}{\rho V} = \rho_l \frac{V_l}{\rho V} \tag{4.2}$$

With the final notation emphasis is placed on the next assumption; the liquid mass present in the control volume is regarded to be incompressible. Therefore ρ_l is taken constant. The liquid mass fraction is a function of time. The density of the complete mixture; gas, vapour and liquid ρ, is dependent of time, as are the volume occupied by the liquid V_l and the total control volume V. This gives:

$$g(t) = \rho_l \frac{V_l(t)}{\rho(t)V(t)}.$$

The volume occupied by the liquid V_l is given by the following integral:

$$V_l(t) = \int_0^t \frac{4}{3}\pi r^3(t,\tau) J(\tau) V(\tau) d\tau \tag{4.3}$$

where $J(\tau)$ is the nucleation rate per unit volume and $V(\tau)$ is the size of the control

volume, at the moment of nucleation. The volume occupied by the droplets is given by $\frac{4}{3}\pi r^3(t,\tau)$. The function $r(t,\tau)$ describes the radius of the droplet, from its time of creation, $r(\tau_0,\tau_0)$ where this radius is equal to the critical radius as given in equation 3.3, $r(\tau_0,\tau_0) = r^*$, up to the present radius of the droplet at time t. Under the integral the product $J(\tau_0)V(\tau_0)$ acts as a weight function for the contribution of the liquid volume of the droplets created at time τ_0 to the total amount of liquid formed at time t. The liquid mass fraction now becomes:

$$g(t) = \rho_l \frac{\int_0^t \frac{4}{3}\pi r^3(t,\tau) J(\tau) V(\tau) d\tau}{\rho(t) V(t)}$$

If the considered lump of mass, liquid and gas–vapour mixture, is at rest, or flows along a stream–line, the fraction $\frac{M_v+M_l}{M_a}$ is fixed. This is identical to the assumption that the droplets do not move relative to the surrounding gas mixture. This is known as the no–slip condition in Hill's Method of Moments. This can be expressed as:

$$dM = 0 \Rightarrow M = \rho(\tau)V(\tau) = \rho(t)V(t)$$

The liquid mass fraction can be rewritten (Hagmeijer 2001):

$$g(t) = \rho_l \int_0^t \frac{4}{3}\pi r^3(t,\tau) \frac{J(\tau)}{\rho(\tau)} d\tau.$$

However, the function $r(t,\tau)$ is not readily available in closed form. The droplet growth rate $\frac{dr}{dt}$ is known in closed form. Therefore $g(t)$ is differentiated with respect to time:

$$\begin{aligned}
\frac{dg}{dt} &= \rho_l \frac{d}{dt} \int_0^t \frac{4}{3}\pi r^3(t,\tau) \frac{J(\tau)}{\rho(\tau)} d\tau \\
&= \rho_l \int_0^t \frac{4}{3}\pi 3 r^2(t,\tau) \frac{dr(t,\tau)}{dt} \frac{J(\tau)}{\rho(\tau)} d\tau + \rho_l \frac{4}{3}\pi r^3(t,t) \frac{J(t)}{\rho(t)} \\
&= \rho_l \frac{4}{3}\pi r^{*3} \frac{J(t)}{\rho(t)} + 3\rho_l \int_0^t \frac{4}{3}\pi r^2(t,\tau) \frac{dr(t,\tau)}{dt} \frac{J(\tau)}{\rho(\tau)} d\tau.
\end{aligned}$$

In this analysis, it is assumed, that at the initial time $t = 0$ there is no liquid present in the control volume. A third assumption is that the present droplet growth rate is independent of the present radius of the droplet. This assumption is certainly not true for very small droplets because of the dependency of the surface tension on the droplet radius, however the assumption is valid for droplets with larger radii.

$$\frac{dr}{dt} \neq \frac{dr}{dt}(r(t,\tau)) \tag{4.4}$$

This implies that, the present value of $\frac{dr}{dt}$, the droplet growth rate, is *independent* of its history. So it can be written:

$$\frac{dr}{dt} = \frac{dr}{dt}(t). \tag{4.5}$$

In this case, it is allowed to take the variation of the radius with time out of the integral:

$$\frac{dg}{dt} = \rho_l 4/3\pi r^{*3} \frac{J(t)}{\rho(t)} + 3\frac{dr}{dt}(t)\rho_l \int_0^t 4/3\pi r^2(t,\tau)\frac{J(\tau)}{\rho(\tau)}d\tau.$$

Careful inspection of the right-hand side of the relation above shows, that the original integral has reappeared; but with the power of the radius reduced by one, and multiplied by the power of the function r and the droplet growth rate. Following this observation, it is helpful to employ the following definition of a liquid moment:

$$Q_n(t) \equiv \int_0^t r^n(t,\tau)\frac{J(\tau)}{\rho(\tau)}d\tau.$$

Q_3 is closely related to the liquid mass fraction:

$$g(t) = \rho_l \frac{4}{3}\pi Q_3(t) \Rightarrow \frac{dg(t)}{dt} = \rho_l \frac{4}{3}\pi \frac{dQ_3(t)}{dt}.$$

The variation of this liquid moment $Q_n(t)$ with time is very much similar to expression of $\frac{dg}{dt}$:

$$\begin{aligned}\frac{dQ_n}{dt} &= r^{*n}(t)\frac{J(t)}{\rho(t)} + n\frac{dr}{dt}(t)\int_0^t r^{n-1}(t,\tau)\frac{J(\tau)}{\rho(\tau)}d\tau \\ &= r^{*n}(t)\frac{J(t)}{\rho(t)} + n\frac{dr}{dt}(t)Q_{n-1}\end{aligned}$$

which is a recurrent relation for the differentiation of Q_n. First consider the formulation of the relevant liquid moments:

$$\begin{aligned}Q_3 &= \int_0^t r^3(t,\tau)\frac{J(\tau)}{\rho(\tau)}d\tau \\ Q_2 &= \int_0^t r^2(t,\tau)\frac{J(\tau)}{\rho(\tau)}d\tau \\ Q_1 &= \int_0^t r(t,\tau)\frac{J(\tau)}{\rho(\tau)}d\tau \\ Q_0 &= \int_0^t \frac{J(\tau)}{\rho(\tau)}d\tau.\end{aligned}$$

Inspection of the last moment, Q_0, shows that there is no longer a functional dependence of t in the integral. So the differentiation of this last liquid moment can be expected to be different from the higher liquid moments:

$$\frac{dQ_0}{dt} = \frac{d}{dt}\left(\int_0^t \frac{J(\tau)}{\rho(\tau)}d\tau\right) = \frac{J(t)}{\rho(t)}.$$

This last result is fortunate, as it shows, that the logical expansion defined by the recurrence relation for the liquid moments, is not continued for $n < 0$. So there is no closure problem for the solution of the set of moments. The system of ordinary differential equations, to determine the liquid moment Q_3 now becomes:

$$\begin{aligned}
\frac{dQ_3}{dt} &= r^{*3}\frac{J(t)}{\rho(t)} + 3\frac{dr}{dt}(t)Q_2 \\
\frac{dQ_2}{dt} &= r^{*2}\frac{J(t)}{\rho(t)} + 2\frac{dr}{dt}(t)Q_1 \\
\frac{dQ_1}{dt} &= r^{*}\frac{J(t)}{\rho(t)} + \frac{dr}{dt}(t)Q_0 \\
\frac{dQ_0}{dt} &= \frac{J(t)}{\rho(t)}
\end{aligned}$$

In this system the variables represent the following quantities:

- Q_3 is proportional to the sum of all droplet volumes,
- Q_2 is proportional to the sum of all droplet surface areas,
- Q_1 is proportional to the sum of all droplet radii,
- Q_0 is the present number of droplets.

Now it is assumed that the droplet growth rate $\frac{dr}{dt}(t)$ is given only by the present local thermodynamic and chemical state, and not by the spatial gradients of r in the flow domain. In this case, $\frac{\partial r(t)}{\partial x_i} = 0$. By addition of the product of vector $\underline{Q}$ and the continuity equation for mass, the system of ordinary differential equations above can be rewritten in strong–conservation form:

$$\begin{aligned}
\frac{\partial \rho Q_3}{\partial t} + \frac{\partial \rho Q_3 u_i}{\partial x_i} &= r^{*3}J(t) + 3\frac{dr}{dt}(t)\rho Q_2 \\
\frac{\partial \rho Q_2}{\partial t} + \frac{\partial \rho Q_2 u_i}{\partial x_i} &= r^{*2}J(t) + 2\frac{dr}{dt}(t)\rho Q_1 \\
\frac{\partial \rho Q_1}{\partial t} + \frac{\partial \rho Q_1 u_i}{\partial x_i} &= r^{*}J(t) + \frac{dr}{dt}(t)\rho Q_0 \\
\frac{\partial \rho Q_0}{\partial t} + \frac{\partial \rho Q_0 u_i}{\partial x_i} &= J(t)
\end{aligned}$$

$$g(t) = \rho_l \frac{4}{3}\pi \frac{(\rho Q_3(t))}{\rho}$$

Where x_i and u_i are the spatial coordinates, and the velocity components in spatial direction respectively, r^*, J and $\frac{dr}{dt}(t)$ are given by the laws formulated for the creation and growth of a single droplet. The above set of equations gives the integral properties of the droplet distribution. So details of individual droplets are not available. To be able to compute a radius needed for droplet growth laws, Hill defined (Hill 1966) an averaged radius as:

$$r_{hl} = \sqrt{\frac{Q_2}{Q_0}} \tag{4.6}$$

Reason for application of Q_2 in calculation of r_{hl}, is the dominance of surface effects in droplet growth, hence the application of the integral surface quantity Q_2.

5. Thermodynamic State of Gas–Liquid Mixtures

The change of phase from vapour to liquid releases latent heat to the surrounding mixture. Due to the condensation, the fractions of the gases in the mixtures change. Both processes result in a change of the thermodynamic state of the mixture. To model these changes regard the enthalpy of the mixture:

$$Mh = M_a h_a + M_v h_v + M_l h_l$$

where $h = H/M$ is the specific enthalpy. By application of the previously defined dimensionless mass fraction $g = \frac{M_l}{M}$:

$$h = (1 - g_{max})h_a + (g_{max} - g)h_v + gh_l.$$

Application of the definition of the latent heat $L = h_v - h_l$ and the definition $c_p = \left(\frac{\partial h}{\partial T}\right)_{p,g}$ results in:

$$c_p = (1 - g_{max})c_{p_a} + (g_{max} - g)c_{p_v} + g(c_{p_v} - \frac{\partial L}{\partial T}_p). \tag{5.1}$$

Under the assumption $\frac{p_v}{\rho_v} - \frac{p}{\rho_l} \approx \frac{p_v}{\rho_v}$, a similar expression can be derived for the isochoric specific heat coefficient $c_v = \left(\frac{\partial e}{\partial T}\right)_{V,g}$:

$$c_v = (1 - g_{max})c_{v_a} + (g_{max} - g)c_{v_v} + g(c_{p_v} - \frac{\partial L}{\partial T}_v). \tag{5.2}$$

With these relations for the specific heat coefficients, the gas constant R_{mix} and the dimensionless ratio γ_{mix} can be computed similar to the case of an ideal gas, $R_{mix}(g, L) = c_p - c_v$ and $\gamma_{mix}(g, L) = \frac{c_p}{c_v}$. Both R and γ are now functions depending on the mass fraction g and the relation for the latent heat L. Derived quantities like pressure p and speed of sound c can be shown (Mundinger 1994) to be:

$$p = \rho R(g, l)T \qquad c^2 = \gamma(g, L)\frac{p}{\rho}.$$

6. Model of Inviscid Flow with Condensation

Based on Reynolds numbers for typical flow problem of interest the flow is assumed to be inviscid. The Euler equations are used to describe the flow. Together with Hill's Method of Moments, the models for nucleation and droplet growth and an equation of state they form a closed set of equations:

$$\frac{\partial}{\partial t}\int_V \underline{\phi}' dv + \int_{S=\partial V} \underline{\underline{F}}(\underline{\phi}') \cdot \underline{ds} = \int_V \underline{W}(\underline{\phi}')dv \tag{6.1}$$

where $\underline{\phi}'$ is the vector with the conserved quantities, $\underline{\underline{F}}(\underline{\phi}')$ the flux vector, and $\underline{W}(\underline{\phi}')$ is the source term:

$$\underline{\phi}' = \begin{bmatrix} \rho \\ \rho\underline{u} \\ \rho E \\ \rho Q_3 \\ \rho Q_2 \\ \rho Q_1 \\ \rho Q_0 \end{bmatrix} \quad \underline{\underline{F}}(\underline{\phi}') = \begin{bmatrix} \rho\underline{u} \\ \rho\underline{u}\underline{u} + \underline{\underline{I}}p \\ \rho\underline{u}H \\ \rho\underline{u}Q_3 \\ \rho\underline{u}Q_2 \\ \rho\underline{u}Q_1 \\ \rho\underline{u}Q_0 \end{bmatrix} \quad \underline{W}(\underline{\phi}') = \begin{bmatrix} 0 \\ \underline{0} \\ 0 \\ r^{*3}J(t) + 3\frac{dr}{dt}(t)\rho Q_2 \\ r^{*2}J(t) + 2\frac{dr}{dt}(t)\rho Q_1 \\ r^{*}J(t) + \frac{dr}{dt}(t)\rho Q_0 \\ J(t) \end{bmatrix} \tag{6.2}$$

where $\rho, \underline{u}, p$ are the density, the velocity and the pressure of the mixture. $E = e + \frac{1}{2}\|\underline{u}\|^2$ and $H = E + \frac{p}{\rho}$ are the total energy and the total enthalpy of the mixture. Q_i is the i–th moment in Hill's Method of Moments. The thermal equation of state reads:

$$p = \rho R(g, L)T \tag{6.3}$$

and the caloric equation of state:

$$e = c_v(g, L)T. \tag{6.4}$$

7. Finite Volume Discretization

With the definition of the control volume averaged ϕ_i:

$$\underline{\phi}_i = \frac{1}{V_i}\int_{V_i} \underline{\phi}' dv$$

equation 6.1is semi–discretized as:

$$\frac{\partial \phi_i}{\partial t} V_i + \sum_{j=1}^{n} \underline{f}(\phi_{i,j}) \cdot \underline{s}_{i,j} = w(\underline{\phi}) V_i$$

The summation of discrete fluxes $\sum_{j=1}^{n} \underline{f}(\phi_{i,j}) \cdot \underline{s}_{i,j}$ is computed using an edge–based data structure as described in Jameson (1986), Barth (1989) and Barth (1994). For every edge the indices of the 2 control volumes connected by the edge are stored, as well as the three spatial components of the surface normal vector of the surface between the two control volumes. The length of the surface normal vector is equal to the magnitude of the surface area. This edge–based approach allows for a cell–centered or a vertex–centered use of the original mesh, without significant changes to the flux computation algorithm. The fluxes are computed, by solving a local one–dimensional Riemann problem for every surface using an approximate Riemann solver. This is implemented in the flow solver for edges oriented in every possible direction in three–dimensional space. Two–dimensional problems with meshes in two independent directions can be regarded as a subclass of the full three–dimensional problem. The same holds for quasi one–dimensional or truly one–dimensional flow problems. With proper definition of additional boundary surfaces in the case of quasi one–dimensional flows, all flows can be computed using the same flow–solver regardless of the mesh being fully three-dimensional, two–dimensional or quasi or truly one–dimensional. The preprocessor, to the flow solver, generating the edge–based data structure from the meshes needs only to insert zeros for the edge–related surface normals

in the directions not relevant for the particular mesh. To date, pre–processors have been written for meshes consisting of line elements for one–dimensional meshes, triangular elements for unstructured two–dimensional meshes, quadrilaterals for structured monoblock two–dimensional meshes, and tetrahedral elements for three–dimensional meshes. However, the edge–based data structure allows simple extension to multiblock meshes, meshes constructed by hexahedra and hybrid meshes. This requires only the pre–processor for the particular element(s) to be developed, and minor additions to the domain boundary treatment in the flow solver. The flow solver has successfully completed simulations for one–, two– and three–dimensional flows. The great advantage of this approach is that almost all testing during development can be done for flow problems in one and two–dimensions decreasing development time, as formulation of one and two–dimensional flow problems and generation of one– and two–dimensional meshes is much less time consuming than in the full three–dimensional case. There is a penalty in the case of computation of one– and two–dimensional flows. For the one–dimensional case the momentum fluxes in the two spatial directions perpendicular to the main spatial direction are computed but not used. In the case of the Euler–equations this would result in 66% increased computational expense. In the two–dimensional case this increased computational expense is 25%. In the case of the computation of the Euler–equations and Hill's momentum equations, this computational overhead drops to 28% in the one–dimensional case, and 12% in the two dimensional case. However, the number of grid points for flow problems in two–dimensions and one–dimensions is one and two orders lower respectively. So the computational overhead is completely negligible next to the enormous advantage of simple and faster testing in lower dimensions.

Eigenvalue–analysis Kelleners (2001) of the complete system of Euler–equations with the Hill Momentum equations has shown that the additional eigenvalues due to the Hill equations are all real and have value $\underline{u}$. So the liquid moments $Q_0..Q_3$ are convected downstream along streamlines, and no new acoustic waves are introduced. The computation of the flux is identical to the case of flow without condensation, with only additional transport equations for the liquid moments.

The presence of the source terms in the Hill momentum equations results in the complete system of partial differential equations being a stiff system. Wishing to use an explicit time–stepping method as a relaxation method to compute a steady state, the fact that the system is stiff would lead to an unacceptable small time–step requirement due to the source terms. To circumvent this time–step restriction a fractional time–stepping method is used as proposed by Oran and Boris, Oran (1987) the differential equation of the form:

$$\frac{d\phi}{dt} + f(\phi) = w(\phi)$$

the solution procedure is split into:

$$\frac{d\phi^*}{dt_1} = -f(\phi^n) \tag{7.1}$$

$$\frac{d\phi^{n+1}}{dt_2} = w(\phi^*) \tag{7.2}$$

where the time–step operator for the first step can be any conventional explicit operator, e.g. Euler–forward or Runge–Kutta. The time step–operator for the second time step

needs to be able to cope with the possible large magnitude of the source $w(\phi^*)$, (see Oran 1987; Mundinger 1994)

The two following subsections highlight two topics which require detailed attention in the case of development of a spatial second–order accurate finite–volume method. For other topics like, flux splitting or flux limiting, see Jameson (1995) and Liou (1996).

7.1. *Higher Order Spatial Reconstruction*

To achieve good accuracy on meshes with moderate vertex densities the computational method must be at least second order. Whereas computation of first–order spatial accuracy allows for the storage location of the cell–averaged value to be located anywhere inside the control volume, this point should preferably be located at the geometric center of gravity for higher–order spatial accuracy. Use of the center of gravity circumvents severe penalties to the applicable CFL–number of individual control volumes. Higher–order reconstructions of cell–averaged data should conserve the cell–averaged value. In case of second–order reconstruction it can be proven that use of the center of gravity satisfies this requirement:

$$\underline{u}(\underline{x}) = \underline{u}_{cg} + \frac{\partial \underline{u}}{\partial \underline{x}}_{cg} (\underline{x} - \underline{x}_{cg}) \tag{7.3}$$

where $\underline{u}_{cg}$ is the cell–averaged value positioned at the center of gravity. $\underline{u}(\underline{x})$ integrated over the control volume gives:

$$\frac{1}{V} \int_V \underline{u}(\underline{x}) dv = \frac{1}{V} \int_V \underline{u}_{cg} dv + \frac{1}{V} \int_V \frac{\partial \underline{u}}{\partial \underline{x}}_{cg} (\underline{x} - \underline{x}_{cg}) dv \tag{7.4}$$

The first term on the right–hand side gives the cell–averaged value. The second term on the right hand side is zero. The gradient $\frac{\partial \underline{u}}{\partial \underline{x}}_{cg}$ can be moved in front of the integral. The remaining integral is the static moment about the center of gravity, and necessarily zero. For vertex–centered control volumes, the movement of the cell storage location, from cell-vertex to center of gravity of the control volume, is largest for control volumes at the physical boundaries of the domain.

7.2. *Linear Reconstruction at Domain Boundaries*

The assumption of linear reconstruction in the control volume in the case of second–order spatial accuracy, requires special attention at the domain boundaries. At solid wall boundaries the pressure part of the flux needs to be calculated. Question is, how the pressure must be integrated along the solid wall boundary surface for the resulting flux integral along the complete boundary of the control volume to be of second–order spatial accuracy. It is assumed that fluxes vary linearly over the control volume. Reconstruction of the flux at the solid wall boundary is therefore similar to linear reconstruction from the cell averaged state of the conservative variables throughout the control volume. The latter requires the computation of gradient the $\frac{\partial \phi}{\partial \underline{x}}$ at the center of the control volume. Green–Gauss reconstruction is often used for computation of this gradient Barth (1994); Aftosmis (1995). Green–Gauss reconstruction is easily implemented using the edge–based data structure. Starting point is Gauss' divergence theorem:

$$\int_V \nabla(\phi) dv = \int_s \phi d\underline{s} \tag{7.5}$$

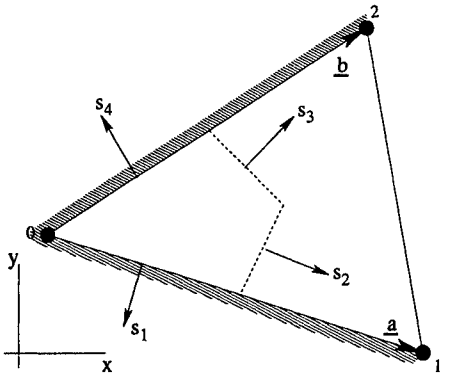

FIGURE 3. Median dual mesh control volume sharing sides with a physical boundary

which is rewritten in discrete form:

$$\nabla(\phi) = \frac{1}{V}\sum_i \phi_i \underline{s}_i \tag{7.6}$$

As an example the linear distribution of ϕ along a domain boundary for a control volume being the median dual to a two–dimensional triangular element is given, see figure 3. The volume V is the surface area associated with vertex 0 in the case of the median dual mesh is:

$$V = \frac{1}{6}\|\underline{a} \times \underline{b}\|$$

To evaluate equation 7.6, the outward pointing surface vectors $\underline{s}_1 ... \underline{s}_4$, and the mean values of the quantity $\phi_1 ... \phi_4$ need to be determined.

$$\begin{aligned}
\underline{s}_1 &= \frac{1}{2}\underline{a} \times \underline{e}_z \\
\underline{s}_2 &= (\frac{1}{3}\underline{b} - \frac{1}{6}\underline{a}) \times \underline{e}_z \\
\underline{s}_3 &= (\frac{1}{6}\underline{b} - \frac{1}{3}\underline{a}) \times \underline{e}_z \\
\underline{s}_4 &= -\frac{1}{2}\underline{b} \times \underline{e}_z
\end{aligned}$$

where $\underline{e}_z = \underline{e}_x \times \underline{e}_y$. ϕ_i is computed similar as would be the case for a median dual mesh volume embedded entirely in the physical domain. The value for ϕ_i at surfaces $\underline{s}_2$ and $\underline{s}_3$ is interpolated:

$$\begin{aligned}
\phi_{\underline{s}_2} &= \frac{1}{2}(\phi_0 + \phi_1) \\
\phi_{\underline{s}_3} &= \frac{1}{2}(\phi_0 + \phi_2)
\end{aligned}$$

At the surfaces $\underline{s}_1$ and $\underline{s}_4$ it is assumed that there exists a linear distribution of ϕ along the surface of the following form:

$$\phi = \omega\phi_0 + (1-\omega)\phi_i$$

The allowable value of ω is between zero and one. Substitution of $\underline{s}_i$ and ϕ_i in equation 7.6 ultimately gives:

$$\nabla(\phi) = \frac{1}{V}\sum_i \phi_i \underline{s}_i =$$

$$\begin{array}{lll} ((3\omega - \frac{3}{2})\phi_0 & +(\frac{5}{2} - 3\omega)\phi_1 & -\phi_2) \quad \frac{1}{a_x b_y - a_y b_x} \begin{pmatrix} a_y \\ -a_x \end{pmatrix} + \\ ((-3\omega + \frac{3}{2})\phi_0 & +\phi_1 \quad +(-\frac{5}{2} + 3\omega)\phi_2) & \frac{1}{a_x b_y - a_y b_x} \begin{pmatrix} b_y \\ -b_x \end{pmatrix} \end{array}$$

To compute the value of ω, the gradient $\nabla(\phi)$ is also computed assuming a linear distribution of ϕ in the triangle given by the vectors $\underline{a}$ and $\underline{b}$.

$$\phi(x) - \phi_0 = \alpha(x - x_0) + \beta(y - y_0)$$

The gradient for this linear distribution is:

$$\nabla(\phi) = \begin{pmatrix} \frac{\partial \phi}{\partial x} \\ \frac{\partial \phi}{\partial y} \end{pmatrix} = \begin{pmatrix} \alpha \\ \beta \end{pmatrix}$$

Using the data in vertices 1 and 2, ϕ_1, ϕ_2 a system can be derived, which can be solved for $\begin{pmatrix} \alpha \\ \beta \end{pmatrix}$. The solution of this system is:

$$\begin{pmatrix} \alpha \\ \beta \end{pmatrix} = \begin{pmatrix} a_x & a_y \\ b_x & b_y \end{pmatrix}^{-1} \begin{pmatrix} \phi_1 - \phi_0 \\ \phi_2 - \phi_0 \end{pmatrix}$$

Both expressions for $\nabla(\phi)$ are equal to one–another. Formulating this identity, and noting that it must be true for any value of ϕ_0, ϕ_1, ϕ_2, it can be shown that:

$$\omega = \frac{5}{6}$$

Returning to the assumption that the wall pressure flux is linearly distributed along the domain boundary surfaces, in a manner similar as any reconstructed scalar ϕ, the weights $\frac{5}{6}$ and $\frac{1}{6}$ can be applied to compute the integral of the pressure over the domain boundary surfaces. E.g. for surface $\underline{s}_4$ this becomes:

$$p_{\underline{s}_4} \underline{s}_4 = (\frac{5}{6} p_0 + \frac{1}{6} p_2) \underline{s}_4.$$

It should be stressed that the value of ω depends on the type of element at the domain boundary, (e.g. triangle, tetrahedron or brick) and the manner in which the control volume is defined (e.g. cell–centered or vertex–centered median dual mesh).

8. Results

The simulation tool described above has been used to compute solutions to flow problems of internal and external flows, adiabatic flows and flows with condensation. The cases presented below have been computed using the following layout of the solution algorithm. Node–centered finite–volume scheme, using median dual mesh cells. Explicit time stepping of the homogeneous equations as described in equation 7.2 using the second order Heun–method. For second order spatial resolution, application of a least–squares

algorithm for computation of spatial gradients in the flow field. Reconstruction of limited second–order states at the control volume interfaces using minimum–maximum restrictions formulated by Barth (1989), and a limiter function by Venkatakrishnan as presented in Aftosmis (1995). Fluxes computed using flux splitting according to Eberle. Computation of the time–updates due to the source terms as mentioned in equation 7.2 using a fractional time stepping method as presented in Mundinger (1994). Inflow boundaries conserving entropy and total enthalpy at infinity upstream for a general equation of state, outflow boundaries maintaining downstream static pressure in case of subsonic outflow, or simple first–order extrapolation of flow quantities in case of supersonic flow. At solid walls application of linear pressure distribution along the outward facing surfaces, as presented in section 7.2. Heat effects due to condensation, are taken into account by inclusion of both the gaseous and liquid phase into the energy conservation equation. This results in strong two–way coupling of the condensation process and the gasdynamics. All computations related to the equation of state, or material properties have been programmed into separate library routines. These libraries are called upon by the routines solving the conservation equations. This produces additional computational overhead, but should allow for quick implementation of different equations of state. In the present form of the flow solver only an equation of state for an ideal gas is implemented.

8.1. *Condensation in Nozzle Ba–120*

Flows with condensation in nozzle Ba–120, designed by Bartlmä, were investigated both experimentally and numerically by Schnerr and co–workers (see Mundinger 1994). Flows for two different humidities are presented in figure 4. The stagnation conditions for both flows in figure 4 are:

$s_0[\%]$	$T_0[K]$	p_0 [pa]
42.1	298.8	100900
49.3	297.1	100900

The expansion of the air–water–vapour mixture gives rise to condensation in the flow field downstream of the nozzle throat. This is seen by the steep rise in the nucleation rate. Following the creation of the nuclei is the process of droplet growth indicated by the rise of the liquid mass fraction $\frac{g}{g_{max}}$. The release of latent heat to the flow, induces a shock in both cases. However the shock-strength in the case of the higher humidity is much larger, and as a result the nucleation pulse is terminated abruptly. In both cases, the continuing expansion due to nozzle divergence results in condensation of almost all of the water–vapour at nozzle station $x = .15[m]$. In the Mach–isoline plot of the flow with higher humidity, the reflection of the curved shock–wave from the nozzle wall is nicely visible.

8.2. *Condensation in Vortex Flow*

To study the process of condensation in vortical flow, a very slender delta wing has been placed inside a tube, see figure 5. At the inlet of the tube a mixture of air–water–vapour flows in at Mach 1.55. The humidity of the mixture at stagnation condition is as low as 1.1%. The wing induces a vortex in the flow field. In the vortex core there is considerable loss of total pressure, clearly visible in figure 6. The vortex spirals downstream in the tube in a helical form. In the low pressure region in the vortex on the upper side of the wing, super–saturation occurs, resulting in large nucleation rate, see figure 7. Note that the region with the highest nucleation rates remains restricted to the front half of the wing close to the apex. This is a consequence of the droplet growth lowering the levels of super–saturation considerably once the first liquid droplets are created in great numbers.

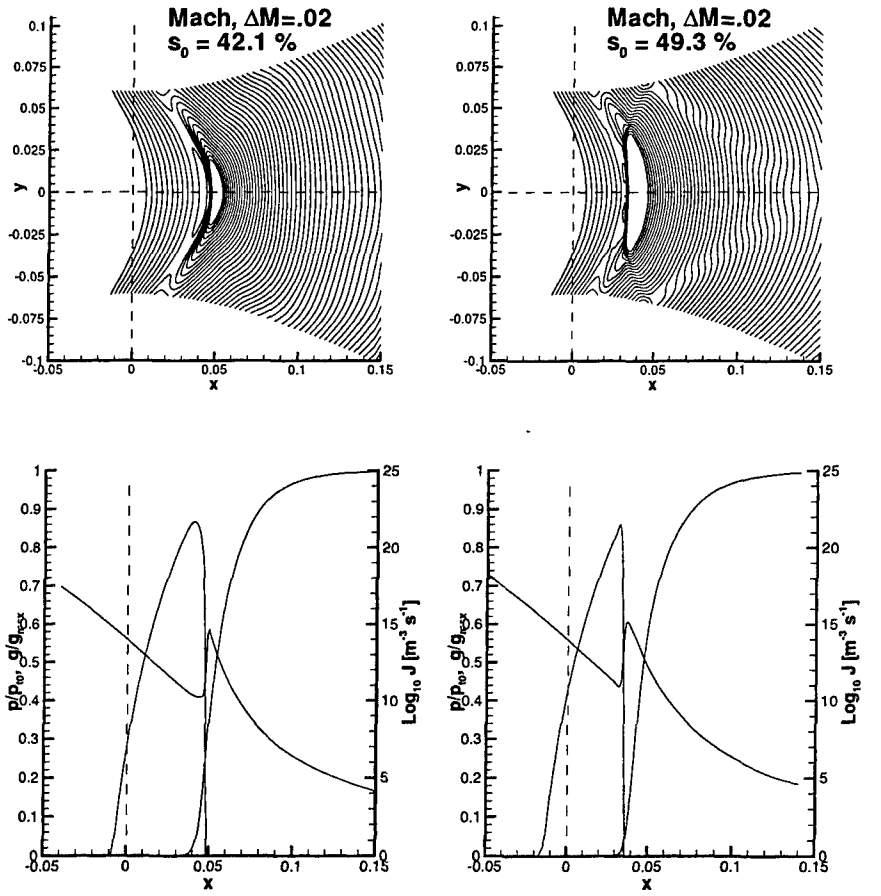

FIGURE 4. Flow with condensation in nozzle Ba120, flow from left to right. Humidity at stagnation condition for left figure: $s_0 = 42.1\%$, right figure $s_0 = 49.3\%$. Mach iso–lines in upper figures, only iso–lines for $M > 1$ are drawn. Nucleation rate J, dimensionless pressure $\frac{p}{p_{t0}}$, and liquid mass fraction $\frac{g}{g_{max}}$ in lower figures. Dashed lines indicate center line, and position of nozzle throat

The dimensionless liquid mass fraction $\frac{g}{g_{max}}$ is plotted in figure 8. On the second half of the upper side of the wing, almost all of the water is present in liquid form. Beyond the trailing edge of the wing, some evaporation of the liquid water occurs, but the main part of the water is convected downstream in liquid form. As the vortex is diffusing over the cross–sections of the tube, so is the cloud of water droplets, as can be noted from the similar shapes of the iso–lines of both the total pressure in figure 6 and the liquid mass fraction in figure 8

9. Conclusions

A brief treatment has been given on condensation in high speed flows. Because of large temperature gradients, the condensation can start well away from thermodynamic equi-

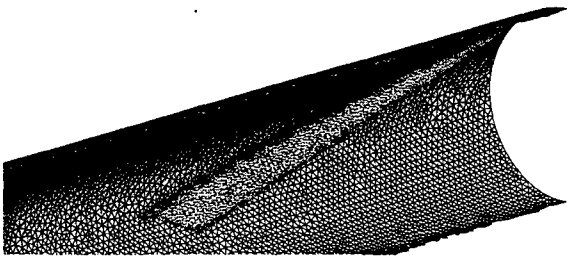

FIGURE 5. Layout of the delta wing, which produces the vortex. For clarity only one half of the tube wall is shown. Flow from upper right corner to lower left corner.

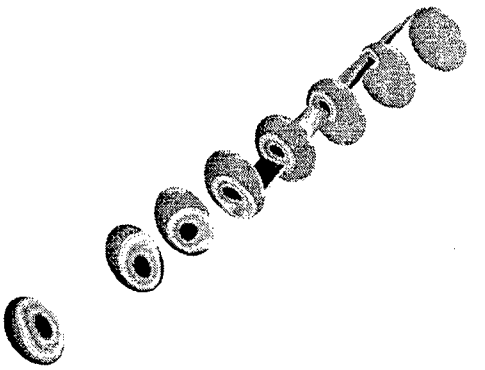

FIGURE 6. Total pressure, p_t

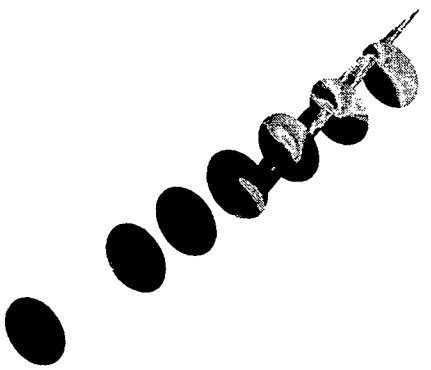

FIGURE 7. Nucleation rate, J plotted on a log–scale.

FIGURE 8. Liquid mass fraction, g.

librium, leading to fog–like clouds consisting of many small droplets. Basic nucleation and droplet–growth models have been presented. A thorough derivation of the integral description of the liquid phase, Hill's Method of Moments has been given. The complete model describing inviscid compressible multi–phase flow with condensation and its finite–volume discretization have been given. Two aspects of the implementation of the finite–volume method for achieving second–order spatial accuracy have been highlighted. Results presented for a two–dimensional flow problem, and a fully three–dimensional flow problem have been computed using one and the same flow solver. The benefit of developing only one single flow solver is clearly felt. From the case of higher humidity in nozzle Ba–120, a strong interaction between gasdynamics and condensation can already be seen. Higher humidities will lead to unsteady flow. Both experimental and numerical data is already available from Schnerr and co–workers. A future extension of the flow solver to take into account unsteady flow should be made. For flows with condensation in vortices simulations should be performed using the full Navier–Stokes equations, to validate the assumption of inviscid flow, made in this work. Improvements must be made with respect to accuracy and robustness of the solution algorithm, to make results of the simulation tool less dependent on grid quality, but the last problem is universal to CFD–methods.

10. Acknowledgments

Thanks are extended to Dr. T. J. Barth of CTR, (Center for Turbulence Research - NASA Ames) for fruitful discussions on consistent reconstruction of higher order spatial states, Dr. N. N. Mansour for creating a productive and enjoyable working environment at CTR, and to Prof. Dr. Ir. H. W. M. Hoeijmakers of Engineering Fluid Mechanics - University of Twente for proofreading of the present work, and continuing support. Funding for this work was provided by RIACS - Research Institute for Advanced Computer Science at NASA Ames Research Center, the JM Burgerscentrum - Research School for Fluid Mechanics in the Netherlands, and TIM - Twente Institute of Mechanics the Netherlands (IMPACT Institute of Mechanics, Processes, And Control - Twente).

REFERENCES

ADAM, S. 1996 Numerische und experimentelle Untersuchung instationärer Düsenströmungen mit Energiezufuhr durch homogene Kondensation, *PhD Thesis*, Universität Karlsruhe (TH), Germany.

AFTOSMIS, M., GAITONDE, D., SEAN TAVARES, T. 1995 Behaviour of Linear Reconstruction Techniques on Unstructured Meshes, *AIAA Journal*, Vol. 33, No. 11, 2038–2049.

BARTH, T.J., JESPERSEN, D.C. 1989 The Design and Application of Upwind Schemes on Unstructured Meshes, *AIAA Paper* 89-0366, AIAA 27th Aerospace Sciences Meeting, Reno, January 1989.

BARTH, T.J. 1995 Aspects of Unstructured Grids and Finite–Volume Solvers for the Euler and Navier–Stokes Equations *VKI Lecture Series* 1994-05, Revised February 1995.

CAMPBELL, J.F., CHAMBERS, J.R., RUMSEY, C.L. 1989 Observation of Airplane Flowfields by Natural Condensation Effects, *AIAA Journal*, Vol. 26, No. 7, 593–604.

DOHRMANN, U. 1989 Ein numerisches Verfahren zur Berechnung stationärer transsonischer Strömungen mit Energiezufuhr durch homogene Kondensation, *PhD Thesis*, Universität Karlsruhe (TH), Germany.

HAGMEIJER, R. 2001 *Private communication*, University of Twente.

HILL, P.G. 1966 Condensation of Water Vapour during Supersonic Expansion in Nozzles, *Journal of Fluid Mechanics*, Vol. 25, part 3, pp. 593–620.

JAMESON, A., BAKER, T.J., WEATHERILL, N.P. 1986 Calculation of Inviscid Transonic Flow Over a Complete Aircraft, *AIAA Paper* 86-0103, AIAA 24th Aerospace Sciences Meeting, Reno, January 1986.

JAMESON, A. 1995 Analysis and Design of Numerical Schemes for Gas Dynamics 1 Artificial Diffusion, Upwind Biasing, Limiters and Their Effect on Accuracy and Multigrid Convergence, *RIACS Technical Report* 94.15, International Journal of Computational Fluid Dynamics, Vol. 4, pp. 171-218.

LAMANNA, G. 2000 On Nucleation and Droplet Growth in Condensing Nozzle Flows, *PhD Thesis*, Eindhoven University of Technology, The Netherlands, ISBN 90-386-1649-X.

LIOU, M.S. 1996 A Sequel to AUSM: AUSM+, *Journal of Computational Physics*, Vol 129, 364–382, Academic Press Inc.

LUIJTEN, C.C.M. 1998 Nucleation and Droplet Growth at High Pressure, *PhD Thesis*, Eindhoven University of Technology, the Netherlands, ISBN 90-386-0747-4.

LUIJTEN, C.C.M., VAN DONGEN, M.E.H. 1999 Nucleation at high pressure. 1. Theoretical considerations, *Journal of Chemical Physics*, Vol. 111, Number 18.

MUNDINGER, G. 1994 Numerische Simulation instationärer Lavaldüsenströmungen mit Energiezufuhr durch homogene Kondensation, *PhD Thesis*, Universität Karlsruhe (TH), Germany.

ORAN, E.S., BORIS, J.P. 1987 Numerical Simulation of Reactive Flow, Elsevier Science Publishing Co., Inc. New York, ISBN 0-444-01251-6.

PRAST, B. 1997 Condensation in Supersonic Expansion Flows; Theory and Numerical Evaluation, Eindhoven: Stan Ackermans Institute, Ontwerpers opleiding Computational Mechanics.

KELLENERS, P.H., PUT, F., HAGMEIJER, R., HOEIJMAKERS, H.W.M. 2001 Development if a Numerical Method for the Simulation of Condensing Real Gas Flows, *ICMF-2001* paper 152, International Conference on Multiphase Flow, New Orleans, May 2001.

SCHNERR, G.H., MEIER, G.E.A. 1996 Control of Flow Instabilities and Unsteady Flows, *International Center for Mechanical Sciences, Courses and Lectures*, - No. 369, Springer Verlag, New York.

WEGENER, P.P. 1969 Nonequilibrium Flows, Part 1, Marcel Dekker, New York and London.